

Yield strength prediction using Dislocation line tension model for age-hardenable Aluminum alloys

B. Tech Project Report

Submitted by

Ripudaman Singh (19118067)

Mayank Verma (19118049)

Under the supervision of

Prof. Sumeet Mishra



Department of Metallurgical and Materials Engineering
Indian Institute of Technology Roorkee

April 2023

Declaration

We declare that this bachelor's thesis entitled "Yield strength prediction using Dislocation line tension model for age-hardenable Aluminum alloys" submitted to Indian Institute of Technology Roorkee is our own original work and has not been submitted in part or in full for any other degree. All sources of information and assistance have been acknowledged and any verbatim statements or paraphrases from the work of others have been cited using the appropriate referencing system.

The authors acknowledge and express sincere gratitude for Ms. Purnima Bharti, Department of Metallurgical and Materials Engineering, IIT Roorkee who performed the experimental work presented in this study. Their extensive knowledge and technical skills were essential to the successful execution of the experiments and the collection of the data presented in this report.

1. Introduction

Aluminum alloys are said to make up 80% of the material used in spacecraft like commercial airplanes and are regarded as one of the most essential materials for the aerospace industry. This can be owed to its low density, high specific strength, excellent ductility and very good manufacturability. They are the prime choice of material for structural applications, e.g. outer fuselage panels, upper and lower wing skins, and wing stringers, etc. Al-Cu-Li alloys have been successfully able to replace the conventional AA-2219 alloy (Al-6 wt.%Cu) for space-related applications such as cryogenic fuel tanks due to its higher strength and lower density. The higher strength of the former alloy is due to the fine dispersion of plate-shaped semi-coherent T1 (Al_2CuLi) precipitates on the $\{111\}_{\text{Al}}$ plane [1].

It is necessary to apply some degree of plastic deformation before the final ageing treatment to ensure the formation of T1 precipitates [2]. The plastic deformation is usually applied via a pre-stretching operation to develop a spatially homogeneous distribution of dislocations, which act as nucleation sites for the precipitates. The evolution of average dislocation density during pre-stretching and subsequent artificial ageing is observed to remain constant with insignificant change even after long-duration artificial ageing treatment [3]. This indicates sluggish recovery kinetics which can be attributed to several factors, such as the high Cu content (~4 wt.%) and segregation of Cu and Mg solutes towards dislocations in Al-Cu-Li alloys [3]. Low level of recovery can have great impact on the final T8 temper (pre-strained + artificially aged) strength as the dislocation density introduced during the pre-deformation will contribute significantly apart from the precipitate-induced strengthening.

Considering the major role of dislocation density on the final T8 strength, many attempts have been made to delineate the strengthening contribution from forest dislocations and T1 precipitates using a linear superposition-based yield strength model [3]. Several studies have shown that linear superposition of strengthening terms is not appropriate, especially when obstacle strength and number densities are comparable [4]. Besides, statistical distribution of obstacles on the slip plane were not considered while computing the individual strengthening contribution. Based on the works

of Foreman and Makin [5] and Nogaret and Rodney [6], it is essential to consider the statistical nature of obstacle spatial distribution on the glide plane for realistic strength calculations.

In the present study, we have employed a dislocation line tension model to calculate the shear resistance of forest dislocations, T1 precipitates and solutes randomly populated on the glide plane. An obstacle strength sensitive superposition law is employed to accurately predict the yield strength evolution of AA 2195 alloy as a function of pre-strain.

2. Theory

The constant line tension model incorporating the circle rolling technique was originally introduced by Foreman and Makin [5]. A variant of this model given by Klahn and Morrison [7,8] is utilized in this study. This model is based on the glide of a single dislocation whose line tension is approximated to a constant $T = 0.5Gb^2$ where G is the shear modulus and b is the magnitude of the Burgers vector. Precipitates, solutes and forest dislocation which are encountered during the glide of a dislocation are collectively termed as obstacles throughout further discussion.

The algorithm involves incremental increase in stress to obtain stable configurations of dislocation corresponding to the applied stress, where a stable configuration at a particular stress τ refers to a state when the dislocation is completely pinned down by obstacles in its path and bows into arcs of radius $R = Gb/2\tau$ between all the pinning obstacles. Whenever the dislocation does not find a stable configuration, the shear stress corresponding to the last stable step is deemed as the critical resolved shear stress (CRSS). A brief description of the simulation algorithm is given below.

A two-dimensional 1 by 1 simulation box is generated with mirror boundary conditions in the x-direction (along the dislocation line) which features N randomly distributed obstacle points (Fig. 1a). The average spacing between every point is

$$L_s = 1/\sqrt{N} \quad (1)$$

and each obstacle has a strength β (or a critical breaking angle φ_c) associated with it, where $0 \leq \beta \leq 1$.

Non-dimensional parameters like length (d^*) and stress (τ^*) are used for overall calculations.

$$d^* = d/L_s \quad (2)$$

$$\tau^* = \tau b L_s / 2T \quad (3)$$

At the start of the simulation, a small stress ($\tau^* = 0.001$) is applied, and in an attempt to find initial pinning obstacles, a circle of radius $R^* = 0.5/\tau^*$ is moved up the left-hand boundary with its center on the boundary itself (Fig. 1b). As mirror boundary conditions are assumed, the dislocation gets pinned by the first encountered obstacle and its image while impinging the boundary at right angle. Then, the circle of the same radius is rotated about the first obstacle anti-clockwise to obtain the next pinning obstacle (Fig. 1c). If no obstacle is encountered while rotating the circle, the first obstacle is deleted from the array along with its image and the circle is moved up along the left-hand boundary for further search. If an obstacle is found during the rotation, geometry conditions are checked for its validity by measuring the angle between the tangents drawn on the two arcs at the initial obstacle (Fig. 1d). If the measured angle is less than its breaking angle $\phi_c = 2 \cos^{-1}(\beta)$, that new obstacle is deleted from the array and the search for the next is continued at the first obstacle itself. Alternatively, if the measured angle is greater than the breaking angle of the first obstacle, the second obstacle is used as the center for further search. This process is continued till the right-hand boundary is reached or the dislocation glides through the whole simulation box. If at a particular step the dislocation line crosses $y = 0.95$ (for a 1 by 1 simulation box), the stress value of the previous step is declared as the critical resolved shear stress.

Simulations performed using the above-described model for 10,000 obstacles of various strengths give a dataset for comparison with theoretical and analytical predictions made in the past which is of our interest (see Figure 4).

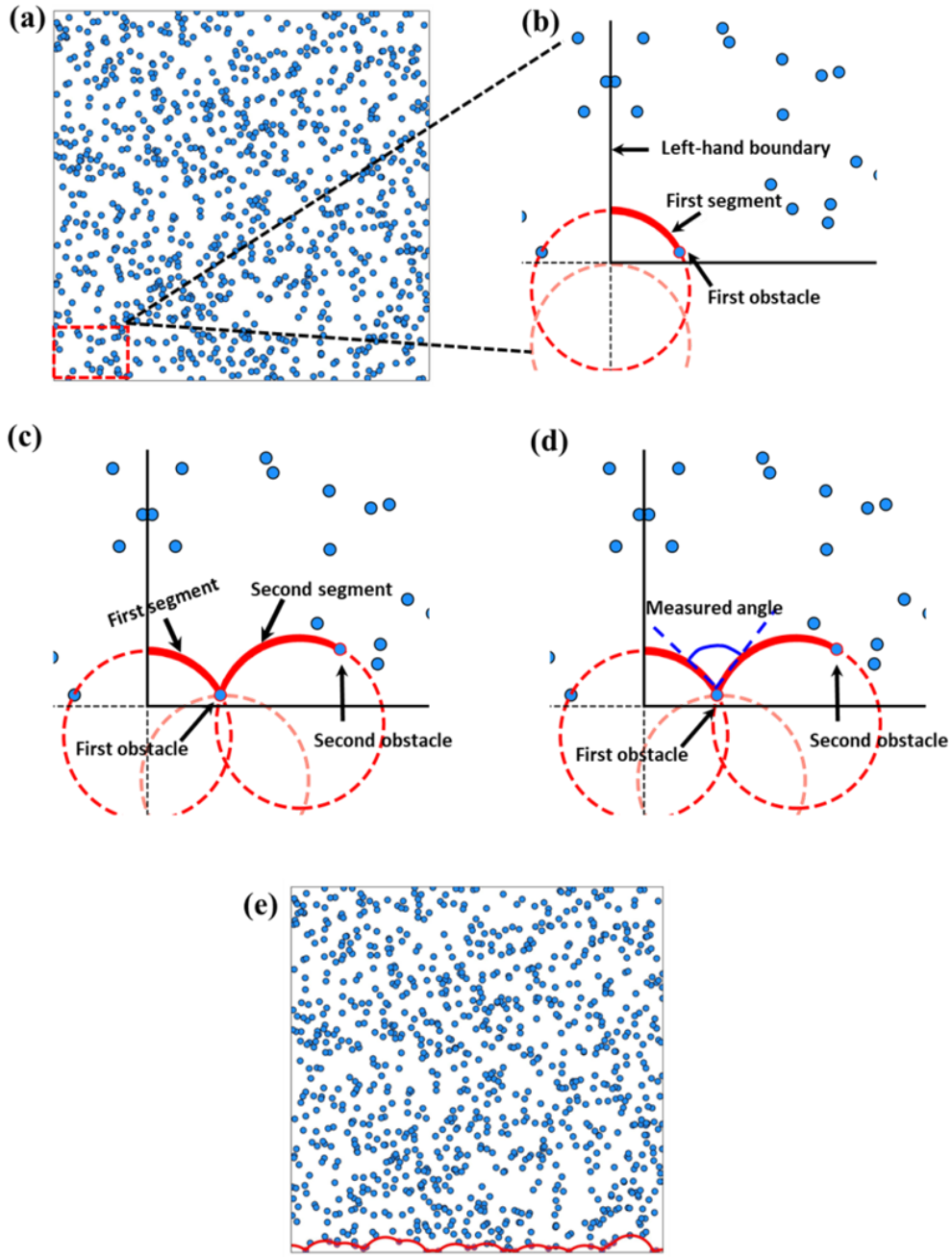


Fig. 1 (a) Simulation box populated with randomly distributed point obstacles (b) Magnified image of the left corner of the simulation box illustrating the process of finding the 1st obstacle and the 1st segment of dislocation by circle rolling (c) Magnified image of the left corner of the simulation box illustrating the process of finding the 2nd obstacle and the 2nd segment of dislocation by circle rolling (d) Measuring the angle constructed by the tangents on the two arcs of the 1st obstacle to check the validity of the 2nd obstacle (e) Stable dislocation configuration extending from the left to the right side of the simulation box for a given value of τ^* .

The CRSS for a regularly arranged square lattice array of obstacles is given by

$$\tau_{sq} = \frac{\mu b}{L} \cos \frac{1}{2} \phi = \frac{\mu b}{L} \beta \quad (4)$$

Friedel [5] showed that the average number of obstacles lying on the dislocation is given by

$$L_{avg} = (\mu b / 2\tau)^{1/3} \quad (5)$$

Using the L_{avg} from equation 5 and replacing it for L in equation 4, we then obtain the Friedel estimate of CRSS.

$$\tau_f = \frac{\mu b}{L} (\cos \frac{1}{2} \phi)^{3/2} = \frac{\mu b}{L} (\beta)^{3/2} \quad (6)$$

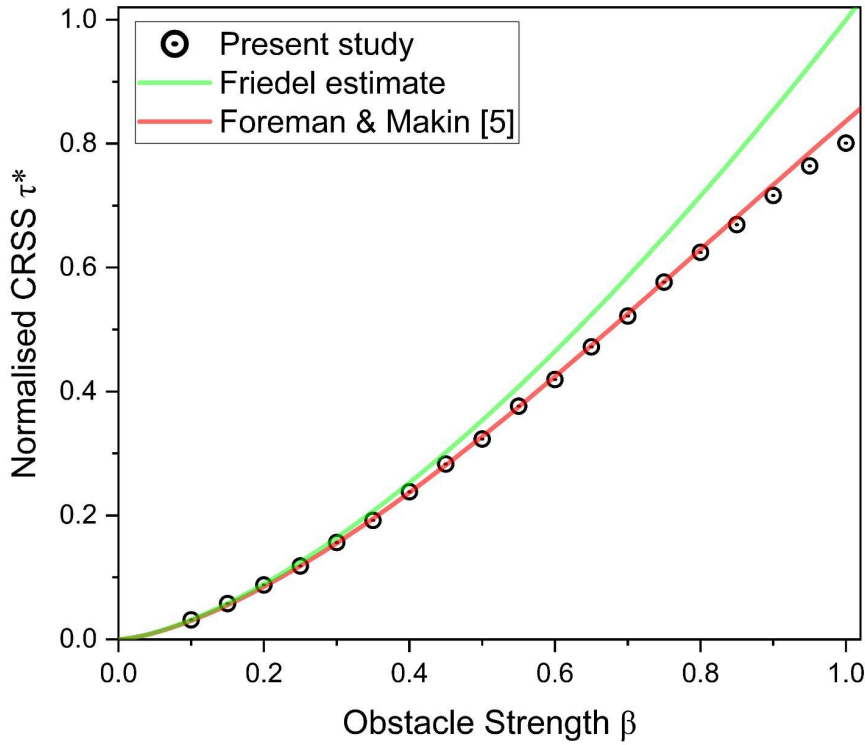


Fig. 2 Simulated critical resolved shear stress (CRSS) of single set of 10,000 randomly distributed obstacles versus their strength

From Figure 2, it can be observed that the Friedel estimate of CRSS follows closely with present computations for weak obstacles ($\beta < 0.4$) and overestimates the CRSS for obstacles lying in the strong regime. Foreman and Makin [4, 5] proposed an empirical law for the normalized CRSS which is in good agreement with our data.

$$\tau_c^* = 0.956 \cos\left(\frac{\phi}{2}\right)^{3/2} \left(1 - \frac{1}{8} \cos\left(\frac{\phi}{2}\right)^2\right) \quad (7)$$

Now, to illustrate the usage of line tension model, simulation of dislocation glide through 800 obstacles corresponding to strong ($\phi_c = 40^\circ$) and weak ($\phi_c = 140^\circ$) obstacle regimes were performed. The last stable dislocation configuration before the dislocation sweeps across the simulation box is shown in Fig. 3 (a-b). It can be observed that the dislocation line remains fairly straight (less curvature) during its motion through an array of weak obstacles. However, the dislocation line developed a significant curvature for the case of the array of strong obstacles. The corresponding shear stress versus shear strain curves are shown in Fig. 3 (c-d). The maxima in these curves correspond to the dimensionless critical resolved shear stress.

The effect of spatial distribution is demonstrated by performing simulations of dislocation glide through an array of two sets of 400 mixed and unmixed obstacles ($N = 2 \times 400 = 800$). For the case of mixed obstacle array, two sets A and B with equal fraction ($f_A = f_B = 0.5$) are completely mixed and populated randomly in the simulation box. Obstacles belonging to set-A (green) are weak with breaking angle $\phi_c = 140^\circ$ and obstacles belonging to set-B (blue) are relatively strong with breaking angle $\phi_c = 40^\circ$. The motion of the dislocation is observed to be uniform, i.e. dislocation encounters and gets pinned by an equal number of obstacles from both the sets. For the case of the unmixed obstacle array, both sets with same volume fraction are not mixed together, rather set-A is restricted in the middle of the simulation box, and the rest of the plane is populated by set-B. The dislocation is observed to prefer gliding through the center of the simulation box which is populated by set-A (weak) obstacles and glides to the top of the simulation box at relatively lower stress than the previous case. This case is analogous for a single set obstacle distribution with sparsely populated region in the middle of the glide plane corresponding to set-A (weak), through which dislocation will be able to traverse relatively easily. The last stable dislocation configuration and shear stress versus shear strain curves for each case is shown in Fig. 4.

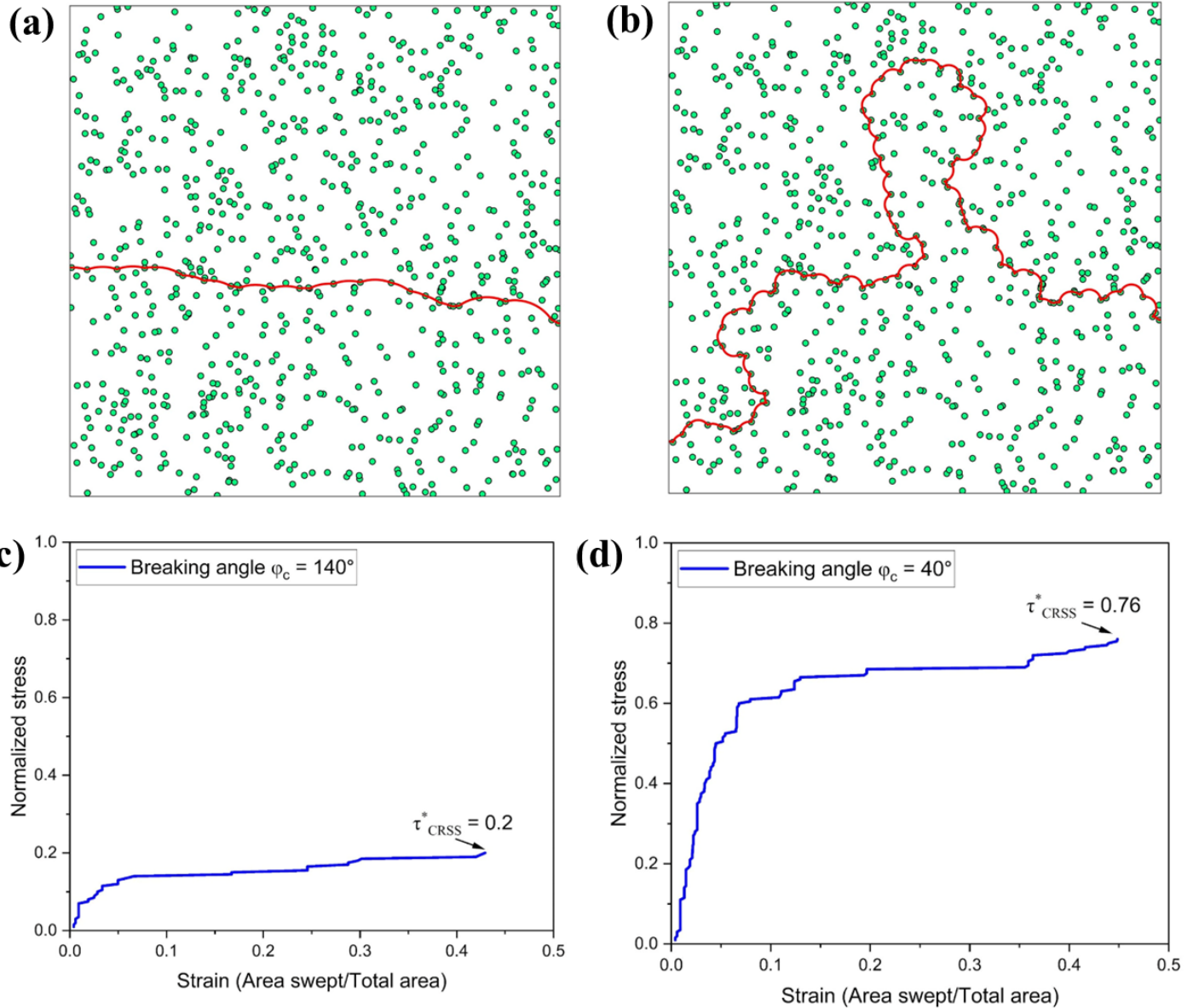


Fig. 3 (a) Last stable dislocation configuration for $\varphi_c = 140^\circ$ (b) Last stable dislocation configuration for $\varphi_c = 40^\circ$ (c) Dimensionless shear stress versus shear strain curve for $\varphi_c = 140^\circ$ (d) Dimensionless shear stress versus shear strain curve for $\varphi_c = 40^\circ$.

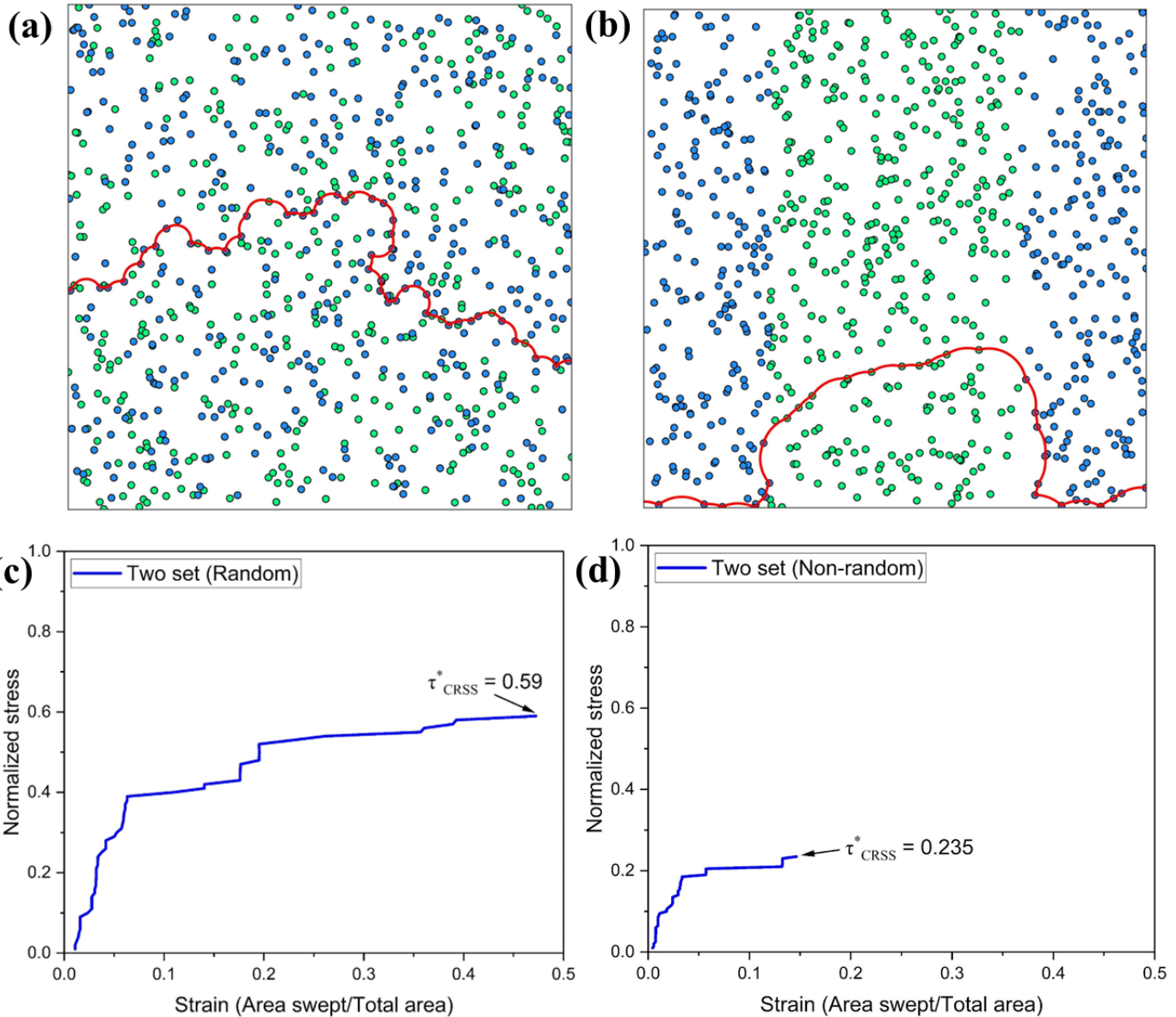


Fig. 4 (a) Last stable dislocation configuration for two sets (mixed) (b) Last stable dislocation configuration for two sets (unmixed) (c) Dimensionless shear stress versus shear strain curve for two sets (mixed) (d) Dimensionless shear stress versus shear strain curve for two sets (unmixed)

3. Experiment Methodology¹

Tensile specimens (Fig. 5a) with a gauge length 25 mm and gauge width 6 mm were machined from the AA-2195 sheets of 1 mm thickness and composition (wt.%) Al-3.7Cu-0.8Li-0.25Mg-0.08Zr0.1Mn-0.25Ag. The tensile samples were annealed at 510°C for 1 h followed by rapid cooling in ice-cooled water to achieve the solutionized condition. The solutionized samples were pre-strained at room temperature to plastic strain values ranging from 5-20%. The pre-strained samples were subjected to artificial ageing at 150°C for 32 h to achieve the peak aged condition. The processing cycle is schematically shown in Fig. 5b.

Hardness and uniaxial tensile tests were performed to determine the mechanical properties of the pre-strained samples. The crystallographic texture of the solutionized sample was determined and the orientation distribution function (ODF) was obtained using MTEX 5.8 software [9]. The microstructures of the pre-strained samples were analyzed using electron backscatter diffraction (EBSD). X-ray diffraction measurements were performed to determine the dislocation density of pre-strained samples. Transmission electron microscopy (TEM) studies were performed to characterize the T1 precipitates in the artificially aged samples.

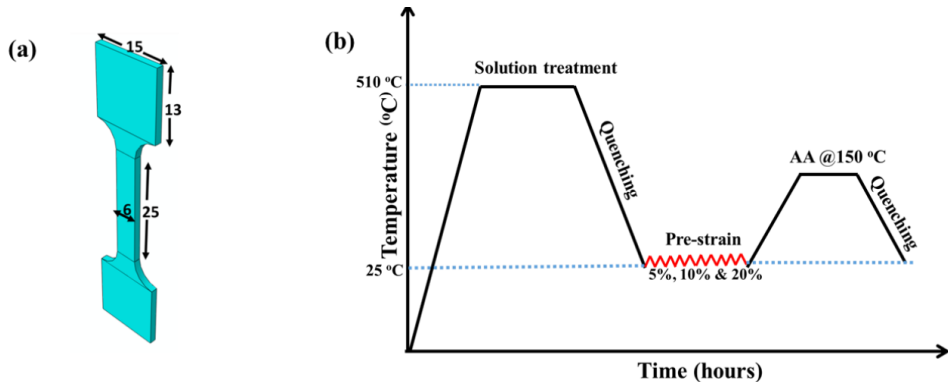


Fig.5 (a) Schematic of the tensile specimen (in mm) (b) Schematic of the processing cycle.

¹ Not performed by the authors. Credit given at the beginning of the report

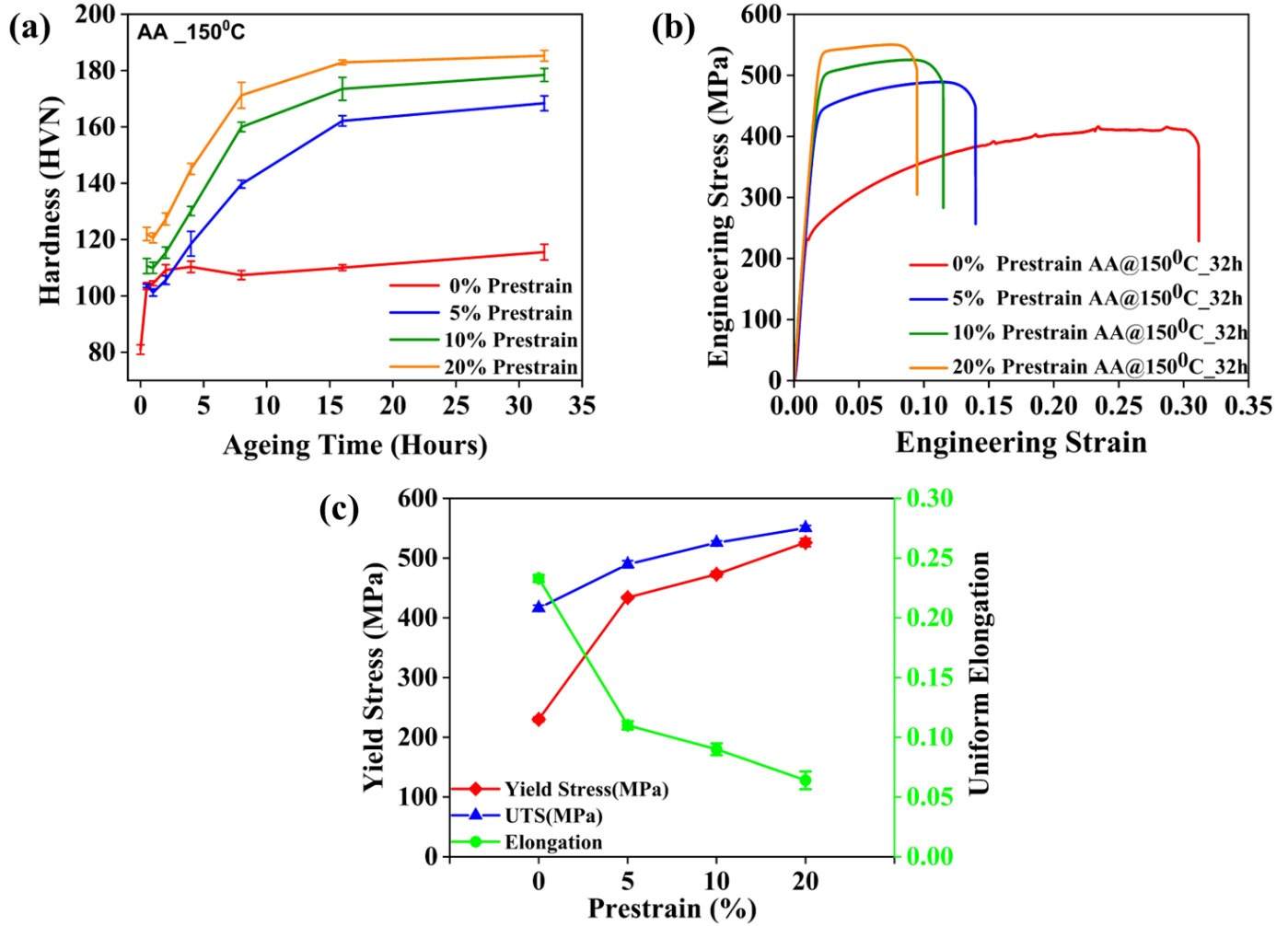


Fig. 6 (a) Evolution of hardness with ageing time ($T=150^{\circ}\text{ C}$) for different pre-strain amount

(b)Engineering stress versus strain curves for different pre-strained peak-aged samples

(c) Yield strength, ultimate tensile strength and uniform elongation as function of pre-strain

4. Results

The age-hardening curves as a function of pre-strain level are shown in Fig. 6a. The curves demonstrate the positive impact of plastic deformation on the ageing behavior. A marked difference in peak hardness can be observed between the pre-strained and undeformed samples. For the pre-strained samples, the peak hardness continued to increase with increasing pre-deformation, although at a decreasing rate. The peak-aged samples (32 h aged) at different pre-strain levels were selected for tensile testing. The engineering stress versus engineering strain curves for the representative samples are shown in Fig. 6b. For the pre-strained samples, the yield strength increased by nearly ~ 100 MPa with an increase in pre-strain from 5% to 20%. The increase in the strength of the pre-strained samples occurred at the expense of ductility. Important results, such as the yield strength, ultimate tensile strength, and uniform elongation are summarized in Fig. 6c.

To estimate the effect of plastic deformation on the dislocation density, X-ray diffraction line profile analysis was performed using the convolutional multiple whole profile (CMWP) fitting software [10]. The evolution of the dislocation density and crystallite size is summarized in Figure 7. It can be seen that the dislocation density increases with pre-deformation, whereas the crystallite size decreases from ~ 690 nm after 5% pre-strain to ~ 150 nm after 20% pre-strain. The dislocation densities for different pre-strained samples are summarized in Table I. It should be noted that the AA-2195 alloy exhibits sluggish recovery kinetics during low temperature artificial ageing at 150°C because of the segregation of Cu and Mg solutes towards dislocations [3]. Therefore, an insignificant change in the dislocation density is expected after artificial ageing of the pre-strained samples.

EBSD studies were performed to observe the meso-scale effect of pre-deformation. Figure 8 shows the inverse pole figure maps (IPFX \parallel tensile axis) after different levels of pre-deformation. After 5% pre-strain, only a few grains (marked by black arrows) illustrate the presence of an orientation gradient. However, with increasing pre-deformation levels, several grains exhibited an orientation gradient indicating heterogeneous deformation.

Pre-strain (%)	Average dislocation density (in pre-strained samples) ($10^{14} m^{-2}$)	Diameter of T ₁ precipitate (nm)	Thickness of T ₁ precipitate (nm)	Number Density of T ₁ precipitate (m^{-3})	Volume Fraction of T ₁ precipitates (%)
5	4.50	42.35±15	1.30±0.40	1.81E22	3.3
10	7.10	37.35±8.8	1.30±0.31	2.52E22	3.5
20	10.5	34.73±9.8	1.30±0.38	2.84E22	3.4

Table I Dislocation density, diameter, thickness, number density and volume fraction of T1 precipitates in different pre-strained samples.

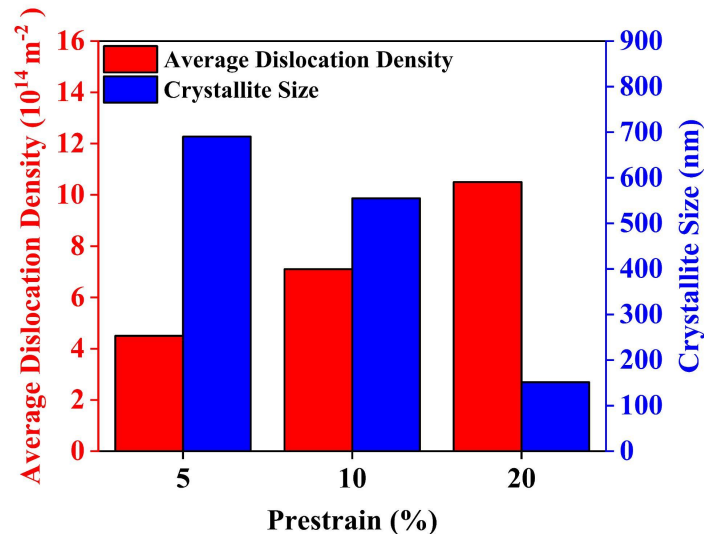


Fig. 7 Evolution of dislocation density and crystallite size after different pre-strain amounts.

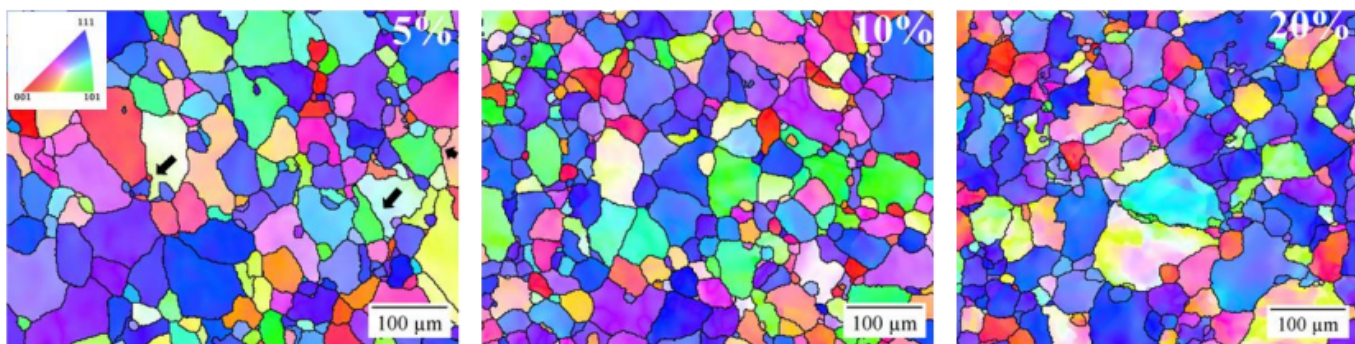


Fig. 8 Inverse pole figure maps after different pre-strain levels

TEM studies were performed to quantitatively analyze the diameter, thickness, number density, and distribution of the T1 precipitates. Figure 9 illustrates representative TEM images taken along the $<110>_{\text{Al}}$ zone axis for different levels of pre-strain. It can be observed that the uniformity of the distribution of T1 precipitates increases with increasing pre-strain level. This can be attributed to the underlying dislocation substructure, where a uniform distribution of dislocations is expected at higher pre-strain levels. Additionally, the average diameter of the T1 precipitates decreases with increasing pre-strain amount. This is due to the higher density of nucleation sites (dislocations) and consequently faster ageing kinetics with increasing pre-strain amount. Important parameters such as the average plate diameter (D), thickness (t), and number density (N_v) are summarized in Table I.

The volume fraction of the T1 precipitates (f_v) was calculated using the following equation 3.

$$N_v = 4f_v/\pi t D^2 \quad (8)$$

The detailed microstructural analysis presented in the above paragraphs to obtain information about the dislocation density and characteristics of T1 precipitates will now be used in the subsequent section to predict the yield strength evolution of AA-2195 as a function of pre-strain.

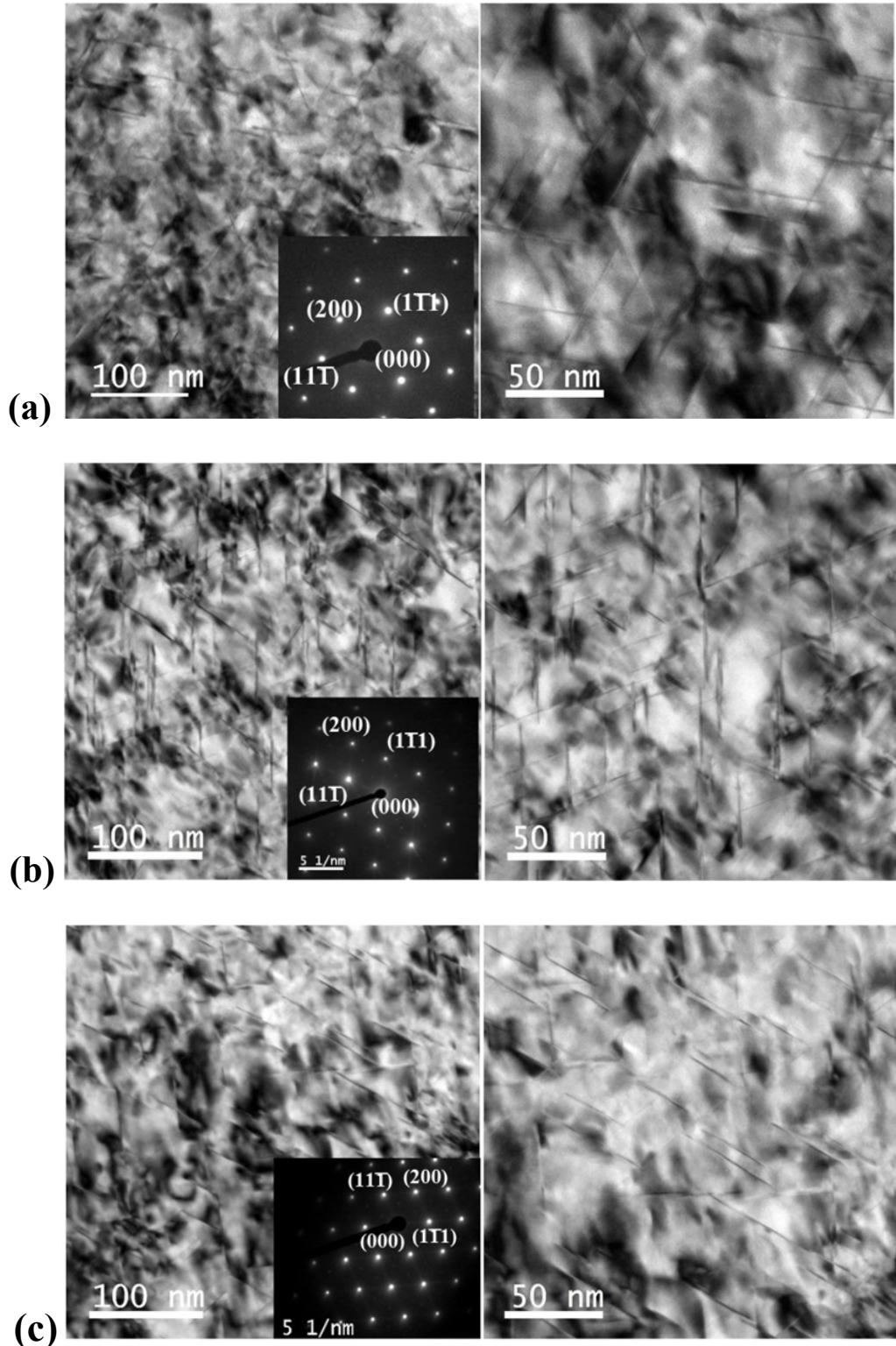


Fig. 9 TEM bright field images for the (a) 5% (b) 10% (c) 20% pre-strained sample aged at 155° C for thirty-two hours with $<110>_{\text{Al}}$ Zone axis

5. Modeling and Discussion

The yield strength of an age-hardenable Aluminum alloy with three types of obstacles (T1 precipitates, forest dislocations, and solutes) can be expressed by a flow-stress superposition law [4].

$$\sigma_{yield} = \sigma_{gb} + \left[\left(\sigma_{sol}^q + \sigma_{ppt}^q \right)^{n/q} + \sigma_{dis}^n \right]^{1/n} \quad (9)$$

Here, σ_{gb} , σ_{dis} , σ_{ppt} and σ_{sol} are the strengthening contributions from grain boundaries, forest dislocations, T1 precipitates, and solutes respectively. Equation 9 reduces to the linear superposition of the flow stress if both the exponents ‘ q ’ and ‘ n ’ are taken as 1. If we take ‘ q ’ and ‘ n ’ as 2, Equation 9 reduces to the quadratic superposition law. Vaucorbeil et al. [4] suggested that the extreme values of ‘ q ’ and ‘ n ’ does not represent the wide range of obstacle strength and densities commonly observed in engineering alloys, so equations based on critical breaking angle of obstacles were proposed to determine the exponents ‘ q ’ and ‘ n ’

$$q = 1 + \exp\left(-\beta(\phi_{sol} + \phi_{ppt})^\delta (\phi_{sol} - \phi_{ppt})^{2m}\right) \quad (10)$$

$$n = n_{ppt\sim dis} + (n_{sol\sim dis} - n_{ppt\sim dis}) \sqrt{1 - \left(\frac{2}{\pi} \tan^{-1}\left(\frac{N_{ppt}}{N_{sol}}\right)\right)^2} \quad (11)$$

$$n_{ppt\sim dis} = 1 + \exp\left(-\beta(\phi_{ppt} + \phi_{dis})^\delta (\phi_{ppt} - \phi_{dis})^{2m}\right) \quad (12)$$

$$n_{sol\sim dis} = 1 + \exp\left(-\beta(\phi_{sol} + \phi_{dis})^\delta (\phi_{sol} - \phi_{dis})^{2m}\right) \quad (13)$$

Here, ϕ_{sol} , ϕ_{ppt} and ϕ_{dis} are the critical breaking angles of the solutes, T1 precipitates and forest dislocations respectively. The parameters β , δ and m are constants with values of 0.1, 1 and 1 respectively [4]. N_{ppt} and N_{sol} are the areal densities of precipitates and solutes, respectively.

The strength (F_{ppt}) of the T1 precipitates obtained using force balance is related to its critical breaking angle (ϕ_{ppt}) as

$$F_{ppt} = 2T \cos\left(\frac{\phi_{ppt}}{2}\right) \quad (14)$$

Here, T is the line tension, which can be approximated as $0.5Gb^2$, where G (25400 MPa) is the shear modulus and b (0.286 nm) is the Burgers vector. The expression given by Dorin et al. [11] for obstacle strength (F_{ppt}) is

$$F_{ppt} = \left[\frac{\pi \times \cos\omega \times \sin\theta \times b \times D}{2t} \right] \times \gamma_{eff} \quad (15)$$

$$\gamma_{eff} = \gamma_{int} + \left[\frac{t}{2\cos\omega \times \sin\theta \times b} - 0.5 \right] \times \gamma_{sf} \quad (16)$$

Here, D is the average diameter and t is the thickness of the T1 precipitates, γ_{int} (0.085 Jm⁻²) is the interfacial energy between the T1 precipitate and the matrix, γ_{sf} (0.005 Jm⁻²) is the interfacial energy corresponding to the creation of a stacking fault, θ (70.53°) is the angle between the two {111}_{Al} planes, and ω (30°) is the angle between the Burgers vector and the <112> direction [6].

For the three representative conditions (5%, 10% , 20% pre-strained and aged at 150°C for 32h), obstacle strength (F_{ppt}) was calculated using equation 15. Subsequently, the corresponding critical breaking angle (ϕ_{ppt}) was determined using equation 14. Table II summarizes the values of F_{ppt} and ϕ_{ppt} for different conditions. It can be observed that as the T1 precipitate diameter decreases with increasing pre-strain level, hence, the obstacle strength (F_{ppt}) decreases, which in turn increases the critical breaking angle of T1 precipitates. This shows that the shear resistance of the T1 precipitates decreased with increasing pre-strain. The critical breaking angle of the solutes (weak obstacle) was estimated to be ~178° by Vaucorbeil et al. [4]. Using ϕ_{ppt} and ϕ_{sol} , the exponent ‘ q ’ was calculated for different ageing condition via equation 10 (Table II).

Pre-strain	F_{ppt} (N)	φ_{ppt}	q	n_{ppt_dis}	n_{sol_dis}	L_{ppt} (m)	N_{ppt} (m ⁻²)	L_{sol} (m)	N_{sol} (m ⁻²)	n
5%	1.1E-9	118°	1.56	1.84	1.25	3.40E-8	8.63E14	1.04E-9	9.25E17	1.25
10%	1E-9	126°	1.64	1.77	1.25	3.20E-8	9.80E14	1.04E-9	9.25E17	1.25
20%	9.2E-10	130°	1.68	1.74	1.25	3.06E-8	1.06E15	1.04E-9	9.25E17	1.25

Table II Summary of T1 precipitates obstacle strength, T1 precipitates critical breaking angle, superposition parameters, T1 precipitates spacing, areal density of T1 precipitates, solute spacing and areal density of solutes for different pre-strained samples.

Utilizing the critical breaking angle of forest dislocations ($\phi_{ppt} \sim 78^\circ$) obtained by Devincre and Kubin [12] via dislocation dynamics simulations, n_{ppt_dis} and n_{sol_dis} were calculated using equations 12 and 13. The areal densities of the precipitates and solutes (N_{ppt} and N_{sol}) were computed using the following relations [4].

$$L_{ppt} = 0.931 \sqrt{\frac{0.265\pi Dt}{f_v}} \quad (17)$$

$$N_{ppt} = 1/L_{ppt}^2 \quad (18)$$

$$L_{sol} = \frac{3^{1/4}b}{2\sqrt{c}} \quad (19)$$

$$N_{sol} = 1/L_{sol}^2 \quad (20)$$

Here, L_{ppt} and L_{sol} are the mean spacing of the T1 precipitates and solutes respectively. It has been observed via atom probe studies that some amount of solutes (Cu and Li) remain in solution even after 32 h of ageing at 155°C [13]. We have taken the effective solute concentration in the matrix to be 3.4 at% ($c = 0.034$) following the approach of the previous authors [13]. The values of L_{ppt} , N_{ppt} , L_{sol} , N_{sol} and ‘ n ’ are summarized in Table II.

It can be observed that the areal density of solutes (N_{sol}) is significantly higher compared to areal density of precipitates (N_{ppt}). As a result, the square root term in equation 11 can be ignored. Therefore, the exponent ‘ n ’ is governed mainly by the critical breaking angles of the solutes and forest dislocations i.e. n_{sol_dis} .

The dimensionless shear resistance of the T1 precipitates (τ_{ppt}^*), solutes (τ_{sol}^*) and forest dislocations (τ_{dis}^*) were evaluated using dislocation glide simulations employing the line tension model with circle-rolling technique. The simulations were performed for five cases corresponding to breaking angles of 78° (forest dislocations), 178° (solute), 116° (T1 precipitates in the 5% prestrained sample), 126° (T1 precipitates in the 10% pre-strained sample) and 130° (T1 precipitates in the 20% pre-strained sample). It should be noted that for dilute precipitate volume fraction ($f_v \approx 0.03$) i.e. $\frac{D}{2L_{ppt}} < 1$, the T1 precipitates can be approximated as point obstacles [14]. The output of the simulations are shown in Fig. 10 (a-e) in terms of the last stable dislocation configuration before the dislocation sweeps across the simulation box and the dimensionless shear stress versus shear strain curve. The maxima of dimensionless shear stress versus shear strain curve corresponds to the normalized shear resistance (τ^*). It can be observed that forest dislocations exhibit the maximum shear resistance ($\tau_{dis}^* = 0.609$) due to the smaller critical breaking angle. For T1 precipitates, as the plate diameter decreased with increasing pre-strain, the obstacle strength decreased (critical breaking angle increased), resulting in drop in the value of τ_{ppt}^* . The solutes exhibit the minimum shear resistance ($\tau_{sol}^* = 0.002$) due to very high critical breaking angle. The dimensionless shear stress values can be used in the following equations to compute individual strength contributions.

$$\sigma_{dis} = \frac{MGb}{L_{dis}} \tau_{dis}^* \quad (21)$$

$$L_{dis} = 1/\sqrt{\rho} \quad (22)$$

$$\sigma_{ppt} = \frac{MGb}{L_{ppt}} \tau_{ppt}^* \quad (23)$$

$$\sigma_{sol} = \frac{MGb}{L_{sol}} \tau_{sol}^* \quad (24)$$

Here, ρ is the average dislocation density in the different pre-strained samples (Table I) and M is the average Taylor factor. The average Taylor factor (M) was determined using crystallographic texture data of solution-treated sample. Insignificant change in texture during pre-straining is expected as only a small amount of plastic deformation was done.

The strengthening contribution of grain boundaries was calculated using the classical Hall-Petch relationship.

$$\sigma_{gb} = k \frac{1}{\sqrt{d}} \quad (25)$$

Here d is the average grain size ($d = 45 \pm 15 \mu m$) and k (0.065 MPa m^{1/2}) is a material specific strengthening coefficient. The values of σ_{gb} , σ_{dis} , σ_{ppt} and σ_{sol} , ‘ q ’ and ‘ n ’ are summarized Table III. Using these values, yield strength was calculated using equation 9. It can be observed that the line tension model complemented by appropriate values of exponents ‘ q ’ and ‘ n ’ results in an excellent agreement between the experimental and simulated values (Fig. 11a). In contrast, the previous approaches of using linear superposition led to overestimation of the yield strength. (Fig. 11b).

Pre-strain	τ_{ppt}^*	τ_{dis}^*	τ_{sol}^*	\bar{M}	σ_{ppt} (MPa)	σ_{dis} (MPa)	σ_{sol} (MPa)	σ_{gb} (MPa)
5%	0.34	0.61	0.002	3.01	218	283	44	10
10%	0.29	0.61	0.002	3.01	198	355	44	10
20%	0.24	0.61	0.002	3.01	171	432	44	10

Table III Summary of dimensionless shear resistance of T1 precipitates, forest dislocations and solutes, average Taylor factor, precipitate strengthening contribution, forest dislocation strengthening contribution, solute strengthening contribution and grain boundary strengthening contribution for different pre-strained samples.

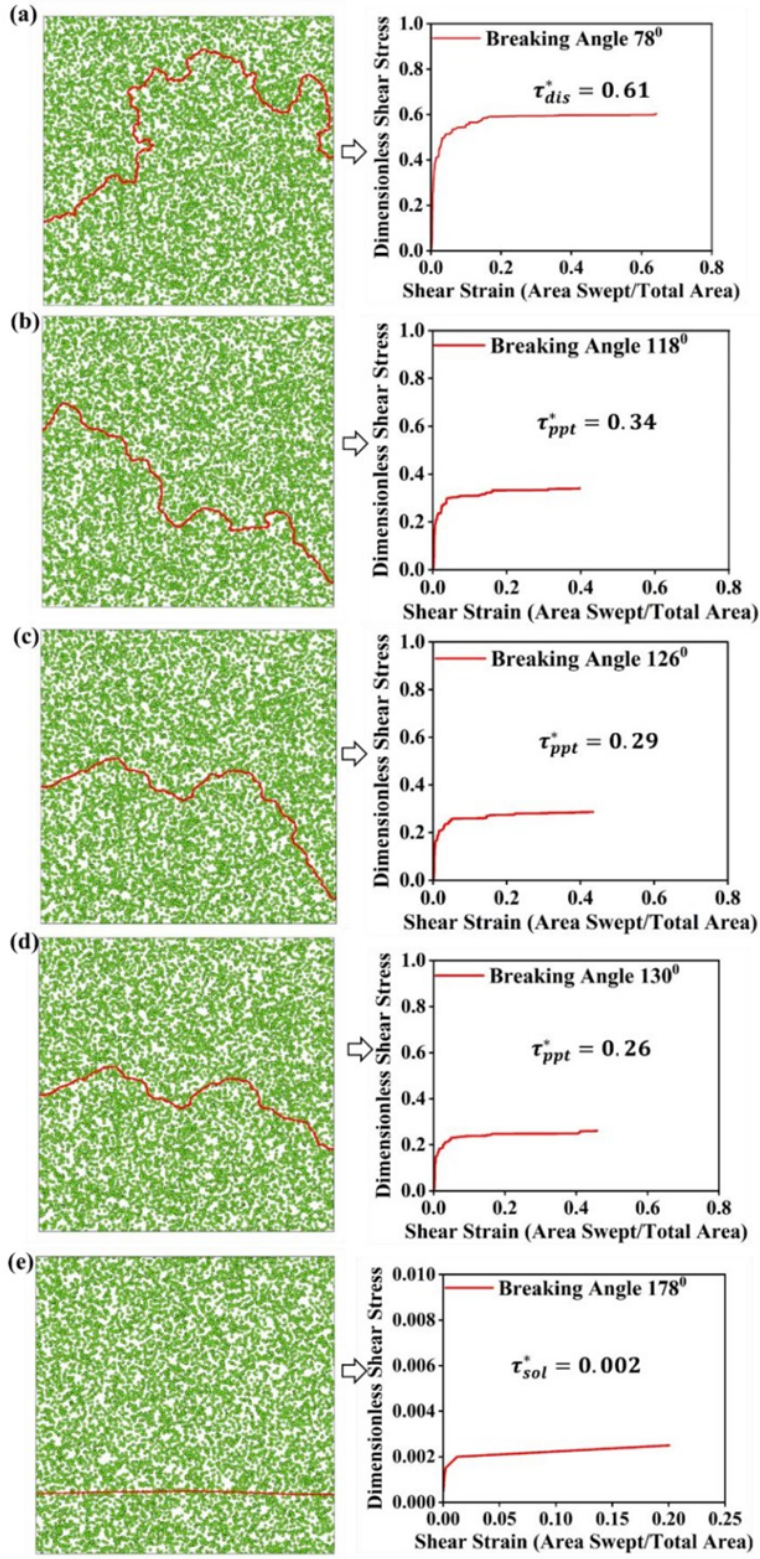


Fig. 10 The last stable dislocation configuration and the dimensionless shear stress versus shear strain curves for different breaking angles (a) 78° (b) 118° (c) 126° (d) 130° (e) 178° .

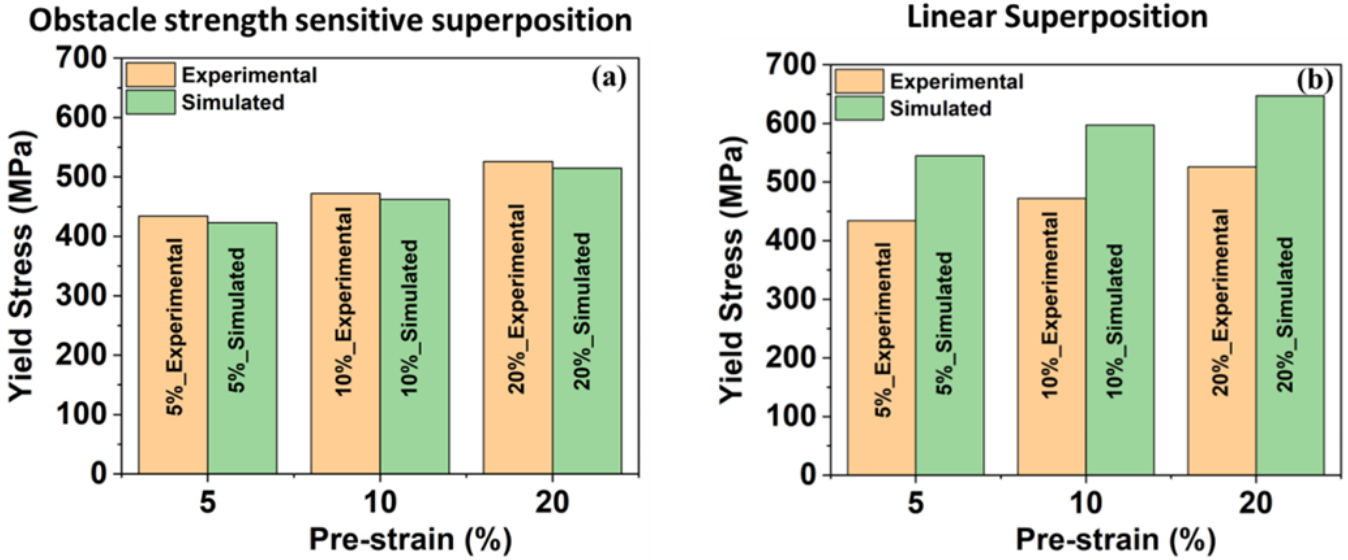


Fig. 11 Comparison between experimental and simulated yield strength values (a) Obstacle strength sensitive superposition (b) Linear superposition

6. Conclusion

- The number density of T1 precipitates increased significantly with an increase in the pre-strain from 5% to 20%. On the other hand, the diameter of the T1 precipitates decreased with increasing pre-strain.
- Dislocation glide simulations revealed that the dimensionless shear resistance of T1 precipitates decreased at higher pre-strain levels owing to a reduction in the diameter of the T1 precipitates (increase in the critical breaking angle).
- Linear superposition led to an overestimation of yield strength
- The yield strength prediction considering the dependence of the superposition exponents ‘q’ and ‘n’ on obstacle strength (critical breaking angles) provided the best agreement with the experimentally observed values.

References

- [1] W. Cassada, G. Shiflet, E. Starke, The effect of plastic deformation on Al₂CuLi (T 1) precipitation, Metallurgical Transactions A 22(2) (1991) 299-306.
- [2] A. Deschamps, B. Decreus, F. De Geuser, T. Dorin, M. Weyland, The influence of precipitation on plastic deformation of Al–Cu–Li alloys, Acta Materialia 61(11) (2013) 4010-4021.
- [3] B. Rodgers, P. Prangnell, Quantification Of The Influence Of Increased pre-stretching on microstructure-strength relationships in the Al–Cu–Li alloy AA2195, Acta Materialia 108 (2016) 55-67.
- [4] A. de Vaucorbeil, W.J. Poole, C.W. Sinclair, The superposition of strengthening contributions in engineering alloys, Materials Science and Engineering: A 582 (2013) 147-154.
- [5] A. Foreman, M. Makin, Dislocation movement through random arrays of obstacles, Philosophical magazine 14(131) (1966) 911-924.
- [6] T. Nogaret, D. Rodney, Finite-size effects in dislocation glide through random arrays of obstacles: Line tension simulations, Physical Review B 74(13) (2006) 134110.
- [7] Morris, J. W., & Klahn, D. H. (1974). Thermally activated dislocation glide through a random array of point obstacles: Computer simulation. *Journal of Applied Physics*, 45(5), 2027–2038.
- [8] Hanson, K., & Morris, J. W. (1975). Estimation of the critical resolved shear stress for dislocation glide through a random mixture of distinct obstacles. *Journal of Applied Physics*, 46(6), 2378–2383.
- [9] F. Bachmann, R. Hielscher, H. Schaeben, Texture analysis with MTEX-free and open source software toolbox, Solid state phenomena, Trans Tech Publ, 2010, pp. 63-68.
- [10] G. Ribárik, B. Jóni, T. Ungár, The convolutional multiple whole profile (CMWP) fitting method, a global optimization procedure for microstructure determination, Crystals 10(7) (2020) 623.
- [11] T. Dorin, A. Deschamps, F.D. Geuser, C. Sigli, Quantification and modelling of the microstructure/strength relationship by tailoring the morphological parameters of the T1 phase in an Al–Cu–Li alloy, Acta Materialia 75(Supplement C) (2014) 134-146.

- [12] B. Devincre, L. Kubin, Simulations of forest interactions and strain hardening in FCC crystals, Modelling and Simulation in Materials Science and Engineering 2(3A) (1994) 559
- [13] B. Gault,F. de Geuser, L. Bourgeois, B.M. Gabble, S.P. Ringer, B.C. Muddle, Atomprobe tomography and transmission electron microscopy characterisation of precipitation in an Al–Cu–Li–Mg–Ag alloy, Ultramicroscopy 111(6) (2011) 683–689.
- [14] A. Argon, Strengthening mechanisms in crystal plasticity, OUP Oxford2007